Light-induced reversible assembly and actuation in ultrafast Ca^{2+}-driven chemomechanical protein networks

Xiangting Lei,[1,*] Carlos Floyd,[2,*] Laura Casas Ferrer,[1] Tuhin Chakrabortty,[1] Nithesh Chandrasekharan,[3] Aaron R. Dinner,[2] Scott Coyle,[3] Jerry Honts,[4] and Saad Bhamla[1,†]

[1] *School of Chemical and Biomolecular Engineering, Georgia Institute of Technology, Atlanta, GA 30318*

[2] *Department of Chemistry and James Franck Institute, University of Chicago, Chicago, IL 60637*

[3] *Department of Biochemistry, University of Wisconsin Madison, Madison, WI 53706*

[4] *Department of Biology, Drake University, Des Moines, IA 50311*

Programming ultrafast, reversible motions in soft materials has remained a challenge in active matter and biomimetic design. Here, we present a light-controlled chemomechanical network based on *Tetrahymena thermophila* calcium-binding protein 2 (Tcb2), a Ca^{2+}-sensitive contractile protein. These networks, driven by Ca^{2+}-triggered structural rearrangements, exhibit dynamic self-assembly, spatiotemporal growth, and contraction rates up to tenfold faster than ATP-driven actomyosin systems with non-muscle myosin II motors. By coupling light-sensitive chelators for optically triggered Ca^{2+} release, we achieve precise, reversible growth and contractility of Tcb2 networks, revealing emergent phenomena such as boundary-localized active regions and density gradient-driven reversals in motion. A coupled reaction-diffusion and viscoelastic model explains these dynamics, highlighting the interplay between chemical network assembly and mechanical response. We further demonstrate active transport of particles via network-mediated forces *in vitro* and implement reinforcement learning to program sub-second, spatiotemporal actuation *in silico*. These results establish a platform for designing responsive active materials with ultrafast chemomechanical dynamics and tunable optical control, with applications in synthetic cells, sub-cellular force generation, and programmable biomaterials.

I. INTRODUCTION

In recent years there has been significant research focus on chemomechanical materials in which chemical signals drive mechanical and structural changes, often with feedback [1]. Both purely synthetic and bio-inspired materials have been explored, often with the key design goals of on-demand force generation and reversible system self-assembly. Synthetic approaches have, for example, integrated pattern-forming chemical reactions with hydrogels to achieve periodic swelling and force generation [2–6]; however, these motions are typically slow and difficult to control, being entrained by chemical oscillations. Researchers have also explored the light-driven covalent assembly of polymer networks [7, 8], but such structures are typically long-lived and unsuited for dynamic force generation. Additionally, reversible self-assembly has been studied in polymeric and liquid crystalline systems [9–12], although these do not easily allow dynamical force generation and are based on uniform chemical triggers rather than spatial light patterning.

As an alternative to purely synthetic systems, bio-derived chemomechanical materials offer evolved platforms for non-equilibrium force generation. These include cellular and bacterial suspensions [13, 14], cilia carpets [15, 16], and, notably, assemblies of cytoskeletal filaments and motor proteins like actomyosin or microtubule-kinesin mixtures [17–27]. Recent bioengineering of light-sensitive molecular motors enables dynamical control over force generation using spatiotemporal light patterning in cytoskeletal materials [22, 23, 28–36]. However, light-controllable cytoskeletally-derived materials face limitations such as flows constrained to filament orientations, low contractility speeds, and reliance on complex molecular bioengineering. To our knowledge no synthetic or bio-derived material has yet demonstrated the simultaneous combination of reversible self-assembly triggered by spatial light patterning, on-demand and reorientable force generation, fast (sub-second) dynamics, a bioorthogonal energy source, and minimal fabrication complexity. A material with these properties would be an excellent candidate for application in synthetic cell biology, in which light-activated rapid force-generation could be used to guide intracellular dynamics.

While most biomechanical processes are powered by a direct coupling between hydrolysis of adenosine triphosphate (ATP) and molecular motion, nature has also developed alternative paradigms for generating biological motion [37–39]. In various heterotrich ciliates, contractile motion arises from specialized Ca^{2+}-binding proteins assemblies which in different organisms have been termed myonemes [37, 40] and spasmonemes [39, 41]. Our comparative genomics analyses reveal sequence similarities among these various contractile proteins (SI I A). Unlike traditional cytoskeletal systems, these Ca^{2+}-based contractile systems generate motion through direct, reversible Ca^{2+}-induced structural rearrangements of the polymers [42], rather than through relative sliding of fila-

* X. L. and C.F. contributed equally to this work.

† Correspondence to saadb@chbe.gatech.edu

ment pairs. These systems generate repeatable forces for ultrafast *in vivo* contractions—the fastest known motions in biology [37]—and are roughly ten or more times faster than actomyosin-based networks (see Discussion). As a result, these Ca^{2+}-powered protein systems hold promise for deriving new biomimetic force-generating materials with faster dynamics than traditional cytoskeletal components.

To begin theoretically understanding their dynamics, in Ref. 43 we modeled protists' myoneme-based contraction *in vivo*, which is triggered by a propagating wave of Ca^{2+} in the cytosol. However, despite this preliminary modeling and related studies [44–49], our quantitative understanding of these naturally evolved protein networks remains limited compared to cytoskeletal systems. Furthermore, experimental methods akin to those used for reconstituting and controlling cytoskeletal materials *in vitro* using spatiotemporal light patterning are currently unavailable for Ca^{2+}-powered proteins. Finally, while theoretical and computational advances have facilitated the design of control strategies for light-triggered cytoskeletal systems [50–57], such methods are currently lacking from our toolkit to study Ca^{2+}-powered protein dynamics.

Here, we purify and reconstitute polymeric networks of *Tetrahymena* calcium-binding protein 2 (Tcb2), a Ca^{2+}-sensitive contractile protein from the ciliate *Tetrahymena thermophila* [58, 59]. Although its physiological function is not fully known, it is thought to play a role in Ca^{2+}-controlled ciliary movement, pronuclear exchange, and Ca^{2+}-mediated signaling in the cortex [58, 60, 61]. This protein is homologous to the Ca^{2+}-binding proteins that underlie ultrafast contraction in other protists, and we focus on it here because there are available molecular tools for its expression and it does not require co-synthesis with a scaffold protein (SI I A).

We develop an experimental methodology to reconstitute a contractile Tcb2 protein network *in vitro* and spatiotemporally control it using light-triggered Ca^{2+} release by diffusing chelators. We show that this system exhibits rich dynamical behaviors, including a Ca^{2+}-driven active region (CAR) near the boundary and a reversal of contractility direction, from radially inward to outward. We explain these dynamics by introducing a continuum model of an overdamped elastic solid with inhomogeneous density and an elastic rest length dependent on the local Ca^{2+} concentration, which we couple with a reaction-diffusion-based description of the chemical components. Additionally, we demonstrate preliminary control over the transport of external particles by the Tcb2 networks *in vitro*, as well as fine-grained control over network contraction *in silico* using reinforcement learning. This system represents a novel biomimetic soft material for producing reversible and rapidly responsive forces at subcellular scales. We conclude by discussing its potential applications in synthetic biology.

II. RESULTS

A. Spatiotemporal light patterning controls Tcb2 protein network dynamics

We first aim to develop an experimental platform for studying ultrafast contractile proteins *in vitro*. The ultrafast contractile motion of protists involves assemblies such as myonemes, and it is driven by rapid waves of Ca^{2+} released from internal stores such as the endoplasmic reticulum (ER) [37, 43, 49]. After the organism contracts, ATP is hydrolyzed to pump Ca^{2+} back into the ER to reset the process. Several protist species in the "atlas" of ultrafast cells exhibit high-speed contraction [62], but they are not model biological systems and, hence, we currently lack sufficient experimental protocols to study them using protein reconstitution. However, homologs of centrin (a main component of myonemes) which also interact with Ca^{2+}, though not observed to produce whole-cell ultrafast cellular contractions, have been identified in other model protists (SI I A). Here, we focus on the homologous protein Tcb2 from *Tetrahymena thermophila* which we show exhibits a marked structural response upon binding to Ca^{2+} [42], making it a valuable model for studying Ca^{2+}-driven contractile proteins. Using available molecular tools we express this protein in ample quantities, allowing for straightforward *in vitro* reconstitution.

Tcb2 is a 25 kDa Ca^{2+}-binding protein found in the cortical layer of *Tetrahymena* [60]. Tcb2 has four EF-hand domains with putative Ca^{2+}-binding sites [42, 58, 63]. In the absence of a solved crystal structure, we use AlphaFold3 [64] to predict the structure of Tcb2 monomers and their conformational changes after binding Ca^{2+}. The predicted conformational changes are consistent with previous NMR data [42] (SI I A), and these conformational changes underscore the potential of using this protein in a chemomechanical material with contractile dynamics.

We clone DNA encoding a synthetic Tcb2 gene that was codon-optimized for bacterial expression into an expression plasmid. We then express and purify the protein from *E. coli* as in Ref. 65 (Methods and SI I C). We observe that purified Tcb2 alone, without additional scaffolding proteins, readily forms fibrous protein networks in response to Ca^{2+} ions and subsequently contracts along the network boundary (SI Video 1, Section 1). Electron microscopy reveals fine, irregular filaments at low Ca^{2+} concentrations (Fig. 1a). At higher Ca^{2+} concentrations we observe denser networks of filamentous protein as shown by fluorescent mCherry-tagged Tcb2 (Fig. 1b). This propensity to self-assemble into a cortex-like [28] network distinguishes Tcb2 from other Ca^{2+}-binding proteins like calmodulin [66].

We employ an experimental methodology that releases Ca^{2+} in a spatiotemporally controlled manner using photolyzable Ca^{2+} chelators. The DMNP-EDTA Ca^{2+} chelator has a photolabile bond, which, when severed

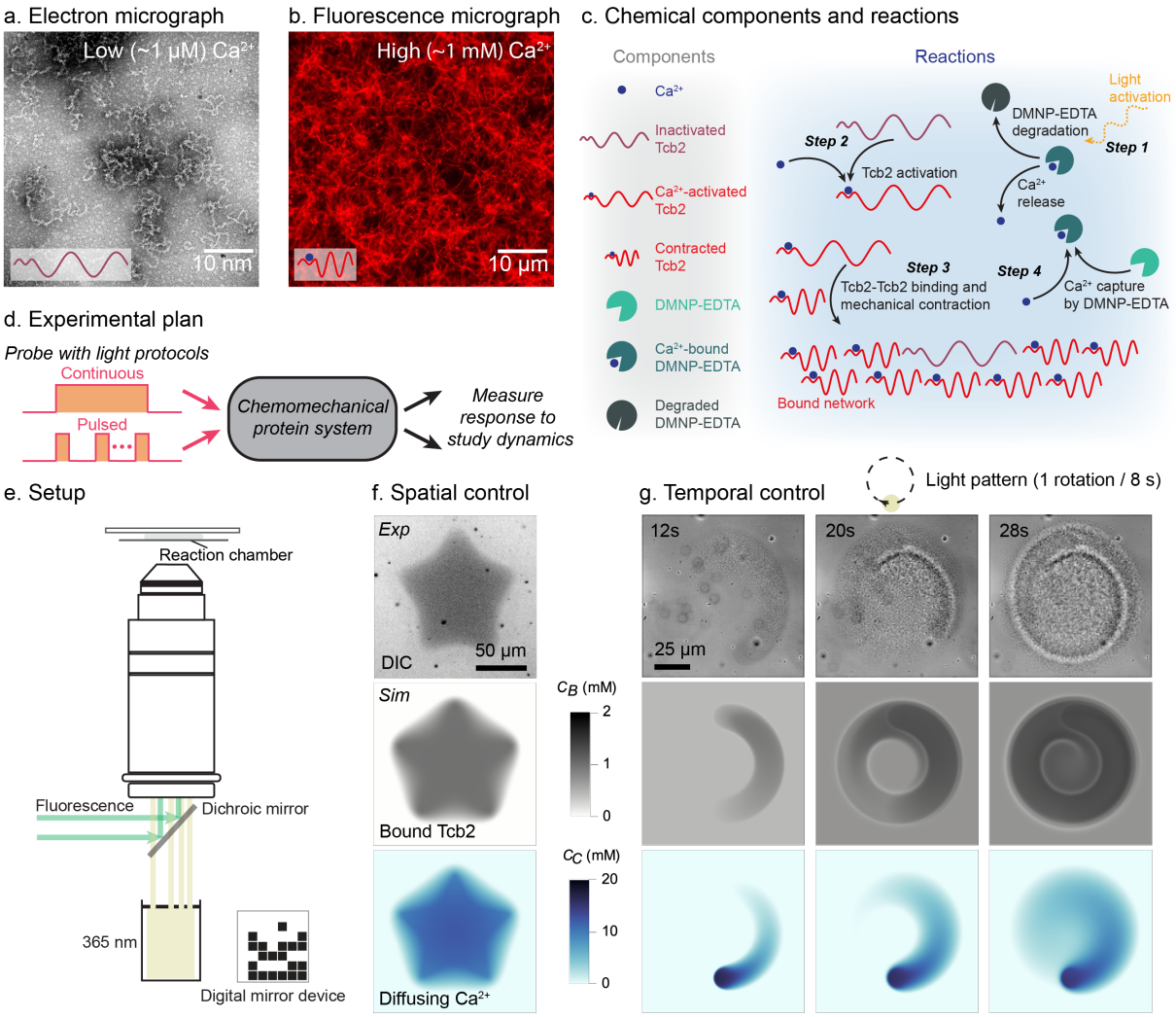

FIG. 1. **Experimental control of Tcb2 network assembly.** (a) Tcb2 filaments observed at $\sim$1 μM Ca^{2+} concentrations using electron microscopy. (b) Tcb2/Tcb2-mCherry filaments in the presence of $\sim$1 mM Ca^{2+} observed via fluorescence microscopy. (c) Chemical components and reactions involving Tcb2 and Ca^{2+}, including light activation, DMNP-EDTA binding/unbinding, and Tcb2 binding/unbinding. (d) Schematic illustration of the experimental plan in this paper. (e) Schematic illustration of the experimental setup. (f) Tcb2 network formation, imaged using DIC, for a star-shaped DMD pattern. Simulated bound Tcb2 (C_B) and diffusing Ca^{2+} (C_C) concentrations are shown below. (g) Dynamic Tcb2 network formation using a cyclic light pattern, with accompanying simulations of bound Tcb2 and diffusing Ca^{2+} concentrations. The light moves in a circle at 0.125 Hz, shown at different cycles.

upon illumination by 365 nm light, releases Ca^{2+} in milliseconds [67] (SI I D). This complex has been used extensively in optogenetics [68–70], and we adapted it here to achieve precise optical control of Ca^{2+} release in Tcb2 solutions. In Fig. 1c we schematically show the chemical components and reactions of the system, including chelators, Ca^{2+} ions, Tcb2 proteins, and externally applied light. Our goal in this work is to use canonical light protocols, such as step functions and periodic pulses, to probe the unknown dynamical properties of this material (Fig. 1d) [71].

To spatiotemporally control DMNP-EDTA photolysis we use a custom optical setup, integrating a digital micromirror device (DMD) pattern illuminator into a microscope (SI I D). This setup uses dual optical pathways via a multi-port illuminator, enabling both fluorescence and 365 nm illumination (Fig. 1e). This system provides sub-micrometer spatial resolution and millisecond temporal precision [72]. To illustrate dynamical control using this system, we project specific spatial and temporal patterns of illumination onto the Tcb2 solution. We illuminate a sharp star shape using the DMD and, within one second, observe a corresponding pattern in the differential interference contrast (DIC) images of the Tbc2 solution, indicating the formation of a Ca^{2+}-bound Tcb2 network at the corresponding location (Fig. 1f). These

patterns can also be programmed into time series, enabling more complex manipulation of the network. We demonstrate this using a circular illumination pattern traveling in a circular trajectory at 0.125 Hz (Fig. 1g and SI Video Section II). We note that the timescale of the observed formation of Tcb2 networks is seconds. This is significantly faster than those observed in actomyosin or microtubule-kinesin systems, which typically require minutes to hours to achieve similar dynamics [31].

We augment this experimental setup with a continuum reaction-diffusion model of the chemical system illustrated in Fig. 1c (Methods and the SI I E). Under reasonable estimates for the unknown model parameters we observe semi-quantitative agreement between the predictions of the model and the experimental measurements of Tcb2 network growth (Figs. 1f,g). We elaborate on details of this model as they become relevant below.

B. A Ca^{2+}-driven active region results from the contraction dynamics of diffusion-limited growth

Having established the experimental and computational setup, we next seek to characterize the chemomechanical dynamics of the Tcb2 solution systematically using standard light activation protocols such as step functions and pulses (Fig. 1d). We first characterize the growth dynamics of the Tcb2 protein network by projecting a sustained circular light pattern on the solution (SI Video Section II). Unless otherwise indicated, all results in this paper use a 75 μm diameter for the illuminated circle, but in SI II A we show results using different illumination diameters. During 100 s of illumination we observe that first, upon illumination, Tcb2 quickly forms a connected network within the illuminated region (Figs. 2a,b), where the Ca^{2+} concentration is suddenly high due to chelator photolysis. Over time the network grows radially outward (Fig. 2a at 100 s and Fig. 2b). In SI Fig. S7 we plot the detected area of the network as a function of time, finding that it scales approximately linearly, which indicates diffusion-limited growth dynamics. The growth rate also increases with the diameter of the illumination region. We additionally observe outward diffusion of Ca^{2+} using rhodamine-2, a Ca^{2+} sensitive dye (SI Fig. S14).

We observe that in the growing network the region near the boundary is mechanically active. The newly formed network at the boundary contracts radially inward, as shown by a kymograph (Figs. 2b,c) and particle image velocimetry (PIV, Fig. 2d). We refer to this boundary as a Ca^{2+}-driven active region (CAR, Fig. 2e) and summarize the processes within the CAR as follows. Chemically, excess Ca^{2+} ions released from photolyzed DMNP-EDTA that have not yet bound to Tcb2 diffuse outward, while unphotolyzed Ca^{2+}-DMNP-EDTA complexes diffuse inward, both following their respective concentration gradients. As these complexes reach the illuminated zone they photolyze and release additional Ca^{2+}, sustaining a loop that fuels network growth by continuously supplying Ca^{2+} from the inside. Tcb2 proteins diffuse inward at the CAR, where they bind to both other Tcb2 proteins and available Ca^{2+}, joining the growing network. Based on molecular size, we estimate the diffusion constant of Tcb2 monomers to be $\sim$100 $\mu m/s^2$, and we show in SI Fig. S21 that accounting for Tcb2 diffusion is necessary to explain the network's growth dynamics. Upon Ca^{2+} binding, Tcb2's rest length shortens, prompting rapid, inward contraction. Since the network's interior has reached mechanical equilibrium, contraction occurs mainly at the periphery.

To describe the contractile dynamics of this system computationally, we augment the chemical variables in the continuum model with a two-dimensional displacement field that obeys the dynamics of overdamped elasticity [73]. We couple this mechanical representation to the chemical fields in two ways. First, because in a typical Ashby plot [74] the elastic moduli of materials increase with their density, we make the elastic moduli of the gel proportional to the local concentration of bound Tcb2. Second, following our previous model [43] for *in vivo* ultrafast myoneme contraction in protists, we decrease the local rest length of the material linearly with the fraction of bound Tcb2 (SI I E).

Using the model, which allows us to resolve all of the chemical components (SI Fig. S12), we observe that the boundary of the Tcb2 network closely follows the diffusing Ca^{2+} profile as shown in Fig. 2f. This supports the picture that the outward growth of the Tcb2 network is driven by the diffusion of Ca^{2+} beyond the illuminated region. The model reproduces the CAR, such that the contracting radial velocity peak is located near the periphery of the Tcb2 network, moving radially outward as the network grows (Fig. 2g). We further find that, to prevent the growth from stalling at finite radius due to the balance of reaction-diffusion fluxes, it is necessary to account for the degradation of DMNP-EDTA chelators in the model (SI Fig. S16).

After the light is turned off in the experiments, Ca^{2+} unbinds from the network and is resequestered by the available DMNP-EDTA chelator. Upon unbinding of Ca^{2+} and re-elongation of the Tcb2 rest lengths, the network quickly relaxes from its contracted state and expands outward (SI Video Section III). It then slowly dissolves via the unbinding of Tcb2 from other Tcb2 proteins. The slow timescale of chemical growth and dissolution is distinct from the fast timescale of mechanical contraction and expansion (SI Fig. S15). A similar interplay between rapid mechanical responses and slower chemical reorganization has been observed in simulations of actomyosin networks under tensile force [75]. We next aim to leverage these two contrasting timescales to overcome the size limitation which arises from the actively contracting region advancing outward in a single sweep and leaving most of the internal region mechanically equilibrated in its path.

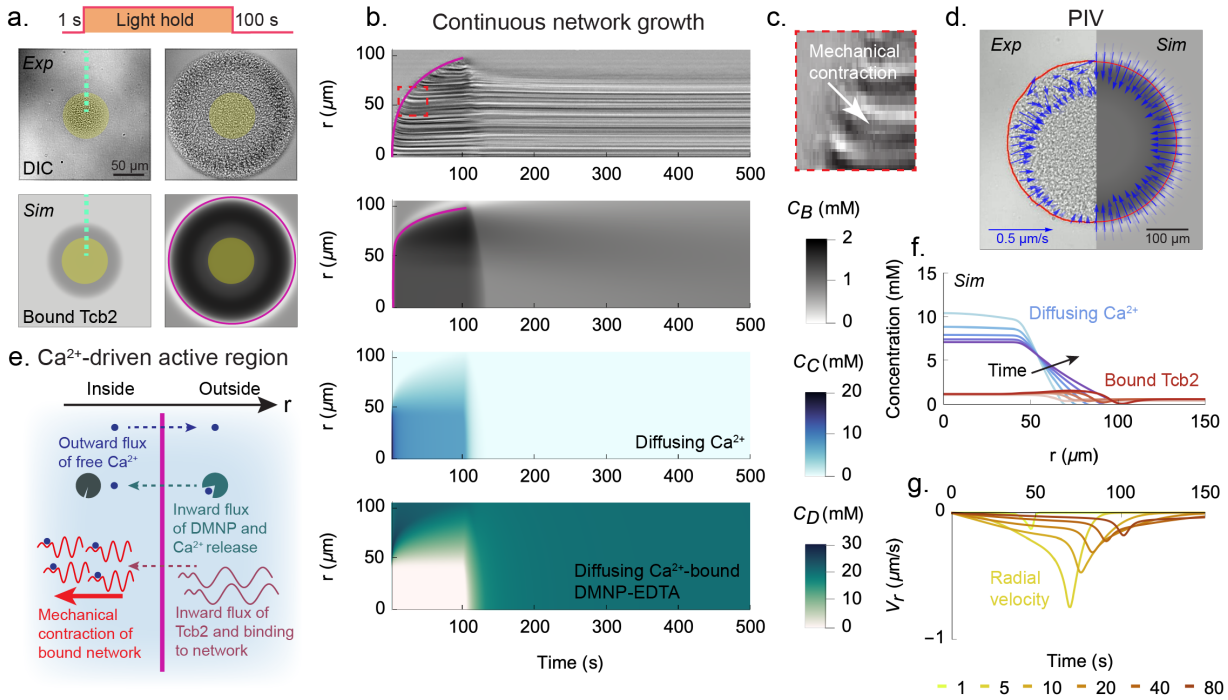

FIG. 2. **Continuous growth of the network produces an active region.** (a) *Top row*: DIC images of Tcb2 network with circular illumination at 1 s and 100 s in a continuous light protocol, using an illumination diameter of 75 μm. Experiment is repeated three times. *Bottom row*: Corresponding Tcb2 simulation images. (b) *First row:* Kymograph constructed from DIC images for the continuous light experiment in panel a, taken along the green dashed line. *Second row*: Simulated kymograph, showing bound Tcb2 concentration as a function of radial position. *Third row*: Same as second row, showing diffusing Ca^{2+} concentration. *Fourth row*: Same as second row, showing Ca^{2+}-DMNP-EDTA concentration. (c) Magnified view of contracting region (red dashed box in the top row of panel b). (d) Experimental PIV field and corresponding simulation image at 100 s. (e) Schematic illustration of the CAR. (f) Concentration of Ca^{2+} (blue) and bound Tcb2 (red) over time. The colors range from light to dark and match the times in the next panel. (g) Radial velocity profiles $V_r(r,t)$ of the network over time.

C. Temporally pulsed illumination yields a larger and faster Ca^{2+}-driven active region

In an effort to "recharge" the system, we next investigate the use of a pulsed, or ratcheting, illumination protocol: a 1 s flash of illumination followed by 29 s of darkness, repeated in cycles. During the initial few cycles, the network formed in the 1 s flash mostly dissolves back into solution during the light-off phase (Fig. 3a at 1 s and 29 s). After these initial cycles, a persistent network begins to form and then grow in size with each subsequent pulse (Fig. 3a at 10th and 30th pulse and Fig. 3b). In SI II A, II H, and II I, we study the dependence of growth dynamics on illumination size, pulse frequency, and DMNP-EDTA concentration.

In Fig. 3c we show PIV measurements comparing the continuous illumination protocol, evaluated at 30 s, with the pulsed protocol, evaluated at the 30th cycle (i.e., the same total time of illumination). In the continuous protocol the CAR is relatively slender and has low average radial velocity (width: $\sim$13 μm, $\overline{V_r}$: 0.21 μm/s), while in the pulsed protocol the CAR is significantly larger and faster (width: $\sim$62 μm, $\overline{V_r}$: 0.52 μm/s); see SI Fig. S17. Importantly, pulsing also causes the CAR to remain large over many repeated cycles (middle row Fig. 3d). To quantify this we measure the width of the radial domain for which the norm of the radial velocity exceeds 0.2 μm/s (chosen as an arbitrary cutoff value), which we plot as a function of time at the bottom of Fig. 3d. These measurements demonstrate that, in contrast to the continuous protocol, pulsed light effectively recharges the system and allows for repeated generation of large contractile forces that act over nearly the whole network.

Simulations semi-quantitatively reproduce these findings (Fig. 3e), allowing closer investigation of the recharging mechanism. Each Tcb2 filament has a rest length that shrinks upon binding Ca^{2+}, supported by earlier NMR data [42] and consistent with structural changes suggested by AlphaFold3 (SI I A). Each filament can thus be viewed as being in one of two states with different rest lengths, depending on whether Ca^{2+} is bound to

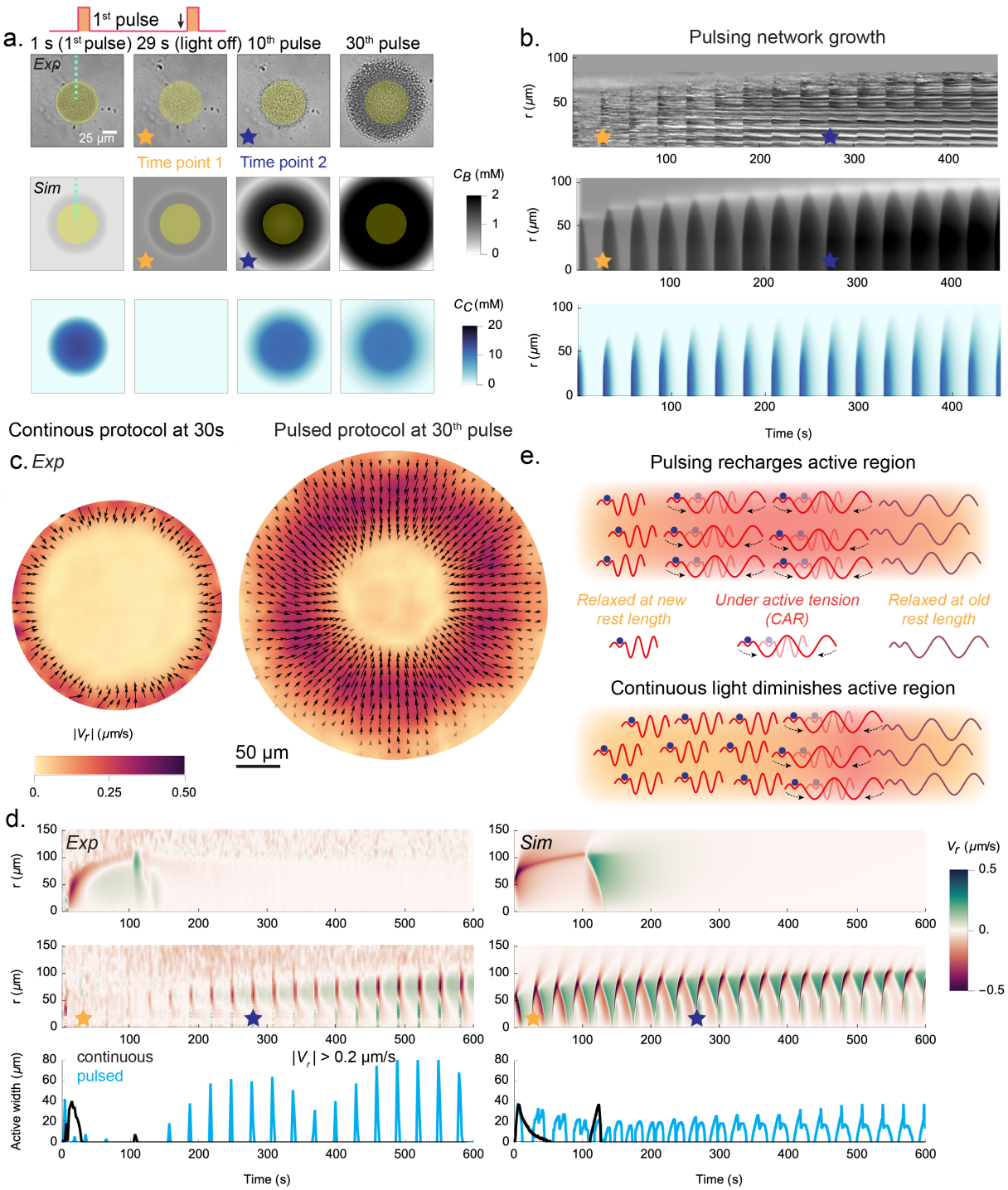

FIG. 3. **Pulsed light allows the CAR to recharge.** (a) DIC images of a pulsed illumination experiment at 0 s, 29 s (right before the 2nd pulse), the 10th pulse, and the 30th pulse. Corresponding simulation images of the bound Tcb2 and diffusing Ca^{2+} profiles are shown below. The blue and yellow stars indicate the same pulses (time points) throughout the figure. (b) Kymographs of the DIC images shown above corresponding simulation results. (c) PIV of continuous light at 30 s (left) and the 30th cycle of the pulsed protocol, with arrows indicating the direction of network motion. The background color represents velocity magnitude and the arrows represent the local velocity vector. (d) *Top row*: Experimental and simulated velocity kymographs for the continuous protocol. *Middle row*: Experimental and simulated velocity kymographs for the pulsed protocol. *Bottom row*: Experimental and simulated plots of the CAR width, defined as the radial extent of the system for which $|V_r| > 0.2$ μm/s, as a function of time for the continuous and pulsed protocols. (e) Schematic illustration of the Tcb2 recharging mechanism. See Fig. 1c for a legend of the molecular components. Experiment is repeated three times.

the filament. Upon Ca^{2+}-binding, but before the filament contracts toward the shorter rest length, there is a build up of mechanical potential energy in the system (SI Fig. S13). The Ca^{2+}-bound filaments then contract in length to reduce this energy. In the pulsed light protocol, the dark phase allows Ca^{2+} to quickly unbind from contracted filaments, restoring their longer rest lengths. The filaments then mechanically relax to these lengths, but due to the slower unbinding of Tcb2 molecules from each other the network does not fully dissolve during the dark phase. In this way the bound Tcb2 state is "ratcheted" while the mechanical state is "reset." The extended Tcb2 filaments are then ready to contract again during the subsequent pulse of light. By contrast, in the continuous protocol the network grows steadily, binding to new Ca^{2+} at the periphery while the interior remains static and stress-free once mechanically equilibrated under the shortened rest lengths. The recharging mechanism in the pulsed protocol enables repeatable sub-second contractile dynamics, offering potential for Tcb2 networks to generate controlled micron-scale mechanical forces using light-based protocols.

D. Spatially heterogeneous patterns of simultaneous contraction and expansion

We observe that during network growth in the pulsed protocol the system not only contracts inward but also exhibits regions that contract radially outward, as shown in the PIV images from the 10th and 25th pulses in Fig. 4a. This is also illustrated in Fig. 4b, which further shows that at even later times (30th pulse) the contraction direction is uniformly radially inward again. This reversal of contraction direction is also observed in the simulations (Fig. 3d).

What causes the change in direction of radial contraction? Analysis of the simulations reveals that a key element is an accumulation of bound Tcb2 near the periphery of the growing network, which appears as a density profile that peaks near the network boundary. In SI Figs. S20 and S21, we show peaked experimental and simulated concentration profiles and demonstrate that boundary accumulation largely depends on the diffusion of Tcb2 inward across the CAR. These new Tcb2 monomers first have a chance to bind when they encounter the network periphery, leading to a build up of concentration there. The dynamical implications of these density inhomogeneities can be understood by considering the new qualitative features of our mechanical model beyond standard linear elasticity, as summarized in Fig. 4c; see SI I E for details. The density of the material is inhomogeneous, which causes the first and second Lamé parameters $\lambda(\mathbf{r})$ and $\mu(\mathbf{r})$ to be inhomogeneous as well, and the instantaneous rest strain tensor $\mathbf{g}(\mathbf{r})$ is also inhomogeneous due to uneven binding of Ca^{2+} to Tcb2. These two modifications produce additional contributions to the total elastic force beyond those in a homogeneous material, and these additional forces depend on spatial gradients in the material density and bound Ca^{2+} concentration. In the presence of a peak in the density of bound Tcb2, these additional forces can overcome the inward contractile force and cause the material to displace up the gradient of material density, which is radially outward for interior parts of the network (Fig. 4d).

To illustrate this picture, we perform reduced simulations in which we turn off chemical reactions, impose a user-defined concentration profile of bound Tcb2 and light-patterned Ca^{2+} activation, and simulate the dynamics of contraction. This allows us to systematically vary the width and accumulation of the Tcb2 profile as an input. The relevant parameters of this setup are illustrated in Fig. 4e (see SI I E for details). The parameter a represents how much accumulation of Tcb2 there is near the boundary of the network. We find that this directly controls the positive component of the radial velocity profile, as shown in Figs. 4f,g, supporting the hypothesis that the accumulation of bound Tcb2 near the boundary underlies the reversal in contraction direction (see Fig. 2a and SI Fig. S20 for experimental observation of accumulation). We further find that as the radius of the Tcb2 network increases beyond the light illumination region, the positive component smoothly decreases to zero in magnitude. This explains why at later cycles in the pulsed protocol, when the network has grown well beyond the illumination zone, the network again contracts uniformly inward. We also find that, as the width of the light activation profile increases, weakening the gradients in rest length, the contractile velocities decrease in magnitude. Finally, increasing the proportionality constant μ_0, which links the shear modulus to the bound Tcb2 density, results in a proportional increase in both positive and negative contraction velocities (Fig. 4g).

Relating these trends to the experiments, during the early pulsed cycles, the contraction direction is inward, as there is little accumulation near the boundary. At later cycles there is appreciable boundary accumulation which leads to regions of both inward and outward contraction. Because the network grows less quickly in the pulsed protocol than in the continuous one it tends to stay more closely overlapping with the illumination zone (shown schematically as blue circles and black squares in Fig. 4g). At late cycles, though, when the network has grown beyond the illumination zone, the contraction direction is predominantly inward again, as predicted by the model. These complex elastic forces suggest a rich design space in which density gradients and Ca^{2+} profiles can be dynamically sculpted to achieve fine-grained spatiotemporal control over the motion of, for example, particles interacting with the Tcb2 network. We next consider strategies for exerting such control.

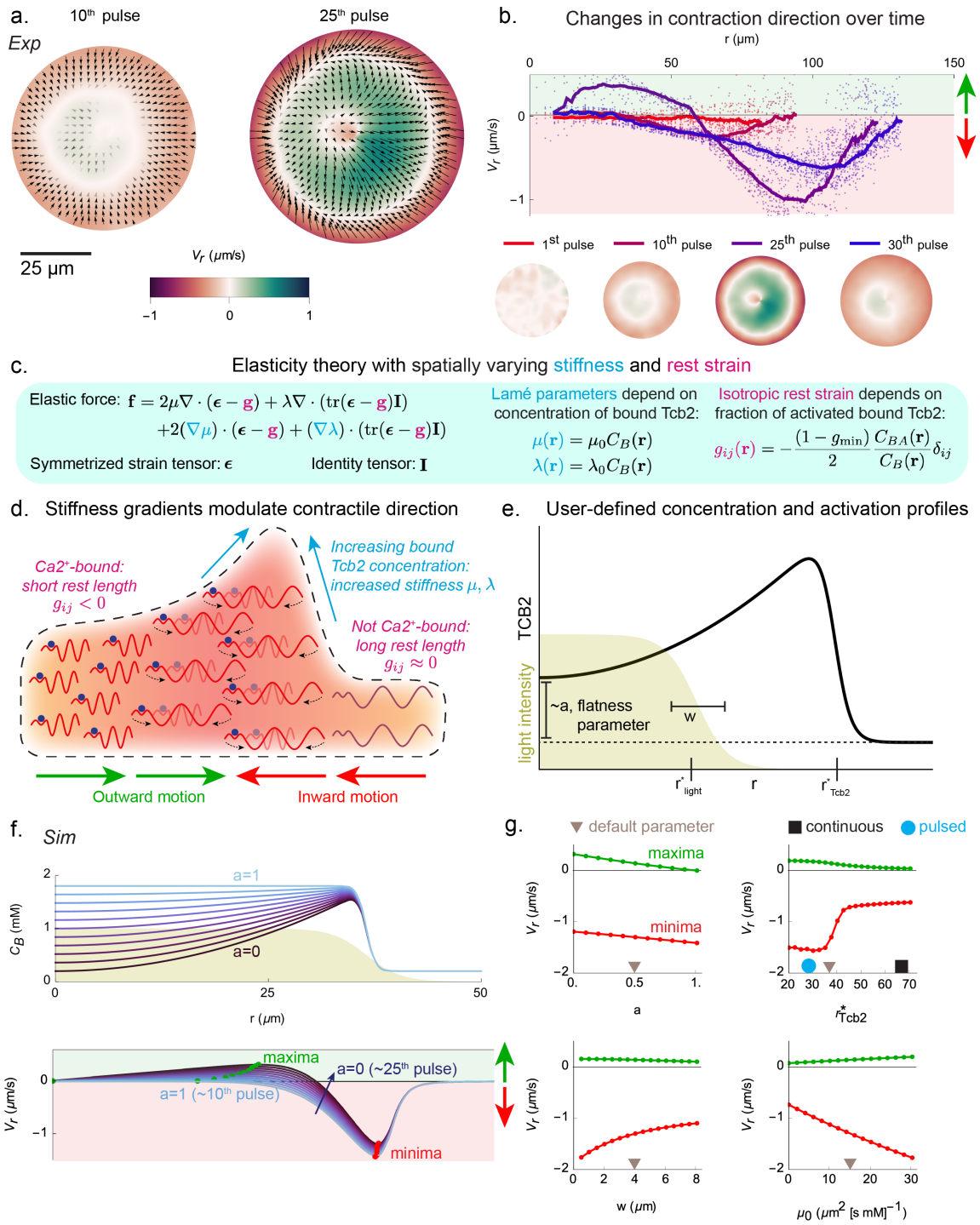

FIG. 4. **Reversal of contraction direction depends on inhomogeneous density.** (a) Experimental PIV images at the 10th and 25th pulses. (b) *Top row*: Velocity profiles at the 1st, 10th, 25th, and 30th pulses plotted against radial distance. *Bottom row*: Experimental PIV fields at the corresponding time points, with the same velocity scale as in panel a. We omit the arrows here for visual clarity and show only color. (c) Summary of the elastic theory used in our model (SI I E for more details). (d) Schematic illustration of the mechanism by which contraction direction reverses due to gradients of stiffness. See Fig. 1c for a legend of the molecular components. (e) Schematic depiction of the user-defined density profile used in the remaining panels. (f) *Top row*: Illustration of the bound Tcb2 profile as the user-defined flatness parameter a (which is small for large boundary accumulation) is varied. *Bottom row*: Radial velocity profiles during light activation for the corresponding density profiles in the top row. Suggestive connections to the pulses in panel b are indicated as corresponding values of a. (g) The maximal and minimal radial velocities (green and red dots in panel f) plotted as a (the flatness parameter), r^*_{Tcb2} (the boundary of the Tcb2 network), w (the width of the light profile), and μ_0 (the slope of stiffness dependence on C_B) are varied. Default values used in the plots are shown indicated with a brown triangle. The black and cyan symbols suggest correspondences to the continuous and pulsed light protocol.

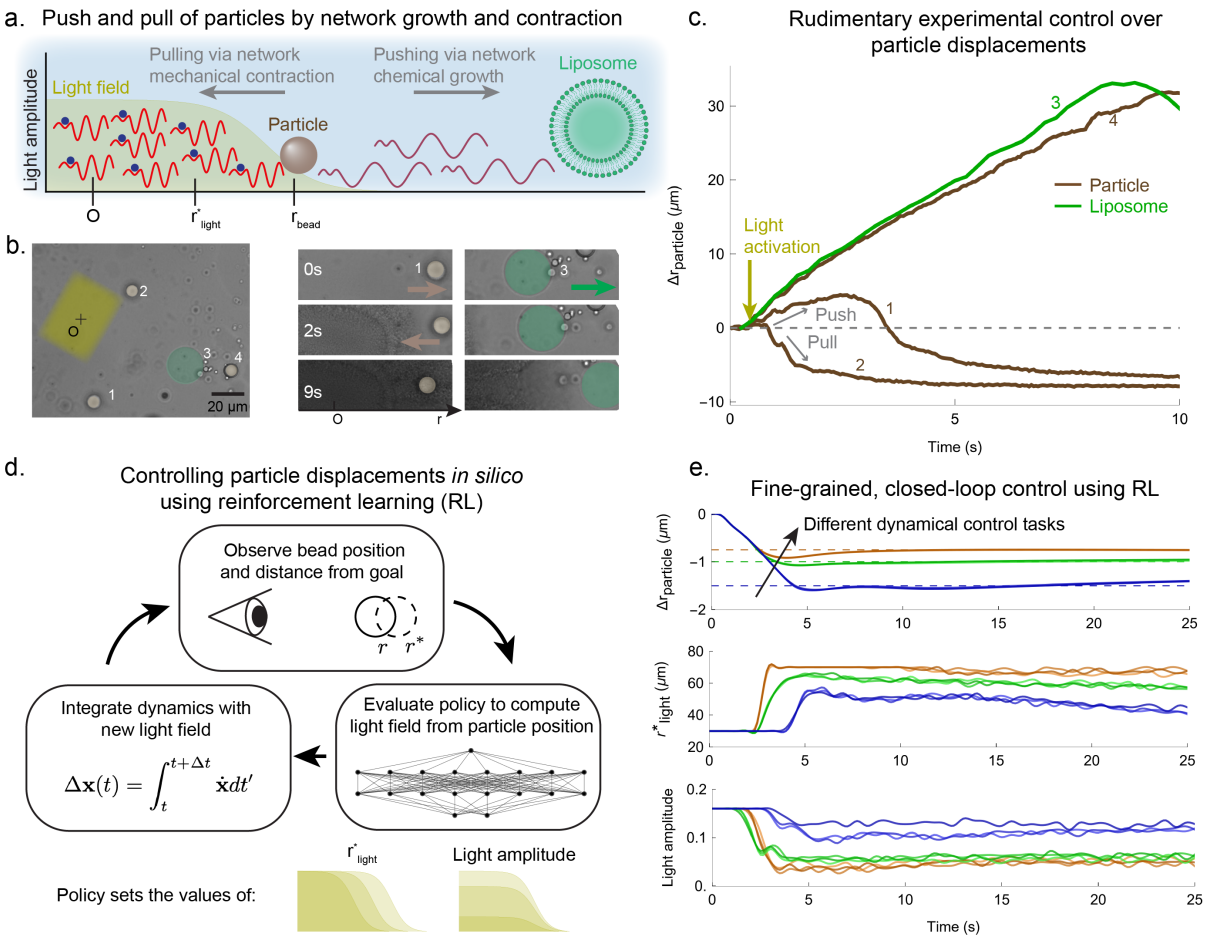

FIG. 5. **Controlling Tcb2 networks to move external particles.** (a) *Top row*: Schematic illustration of the Tcb2 network under light control interacting with particles, such as embedded particles and floating liposomes. (b) Experimental images of the motion of particles and liposomes as the yellow rectanglular region is illuminated continuously. Particles 1, 2, and 4 are lipid particles, and particle 3 is a liposome. (c) Displacements of three particles (brown) and a liposome (green) under light activation. (d) Schematic illustration of the feedback loop for controlling particle displacements *in silico* using RL. (e) *Top row*: Trajectories of the displacements over time for three different dynamical control tasks targeting different displacements. Three iterations near the end of the RL training are shown for each task. *Middle row*: The policy choices for the light position corresponding to the trajectories in the top row. *Bottom row*: The policy choices for the light amplitude corresponding to the trajectories in the top row.

E. Tcb2 network application and control by reinforcement learning

To operationalize the pull and push of Ca^{2+}-driven Tcb2 networks for active transport, we perform experiments in which the networks interact with liposomes, lipid particles (Figs. 5a,b) and polystrene beads (SI Fig. S22 and SI Video VI); see Methods for details on the liposome preparation. We shine light in a fixed region, and the Tcb2 network grows outward and interacts with the lipid particles. Some particles are pulled inwards, some are pushed outwards, and some are first pushed outwards and then pulled inwards (Fig. 5c and SI Fig. S22). Whether a particle moves inward or outwards depends on its initial radial distance from the illumination zone: particles near the zone are enmeshed in the quickly formed network and pulled in as it contracts, while those further away are sterically repelled by the slowly growing Tcb2 network and pushed out (SI Video VI). This suggests a diverse set of options for dynamical control over external objects, although we leave a full exploration of control strategies to future work.

Finally, we aim to test the feasibility *in silico* of closed-loop control for precisely positioning particles using active Tcb2 networks. In simulations, we use reinforcement learning (RL) [76] to learn a policy which maps the current state of the system, the displacement at a position in the network, into a set of choices for the radius and amplitude of a circular light pattern (Fig. 5d). The control task is to bring the displacement to a certain position and then keep it there. Despite the fact that the RL agent only sees a coarse description of the

system state, it is able to learn policies which solve different control tasks (Fig. 5e) [56]. The learned policies first shine the light at high amplitude to grow and contract the network inward, bringing the particle to the desired location, and the light position and amplitude then oscillate and drift to compensate for deviations of the particle from the target. Similar closed-loop control was recently demonstrated experimentally on active nematic channel flow [54]. Our results suggest that Ca^{2+}-driven Tcb2 networks are amenable to control and may, in the near future, be used to exert precise mechanical forces at the micrometer and second scales.

III. DISCUSSION

We have developed an experimental platform and accompanying continuum model to control the Ca^{2+}-driven contractile dynamics of Tcb2 protein networks *in vitro*. By reconstituting these networks outside the protists in which they naturally occur, we decouple them from the cellular complexity and directly manipulate the chemomechanical processes that drive the fastest molecular motions known in biology [37, 62]. Using a light-sensitive Ca^{2+} chelator we locally tune the Ca^{2+} concentration in the solution, allowing us to exert fine-grained spatiotemporal control over the network's growth and contraction. The disparate timescales of these two processes—slow chemical growth and comparatively fast mechanical response—give rise to rich material dynamics. By periodically pulsing light, we can sustain large spatial areas of contractile response for hundreds of cycles through a ratcheting-like effect. Moreover, the repeated mechanical contractions reflect the slowly evolving concentration profile of the growing network, leading to surprising reversals of contraction direction due to strong density inhomogeneities. The dynamical malleability of this system presents an excellent opportunity for generating on-demand micron-scale forces, which we have explored both *in vitro* by moving lipid particles and *in silico* using reinforcement learning.

This biomimetic material is different from reconstituted actomyosin or microtubule-kinesin networks in several ways. First, the Tcb2 networks are largely amorphous and isotropic, such that the direction of contraction is not restricted by the orientation of the filaments [19]. Second, our system exhibits a contraction rate of $\sim$0.5 μm/s, which is an order of magnitude higher than that of actomyosin networks driven by non-muscle myosin II ($\sim$0.05 μm/s) [28, 77, 78], about twice the rate of muscle myosin II ($\sim$0.25 μm/s) [79–81], and comparable to the continuous contraction rate of mixed myosin IIA and myosin IIB networks ($\sim$0.4 μm/s) [82]; see SI S2 for a comparison to specific studies. This system is slower than microtubule-based transport driven by kinesin under light activation, which reaches speeds of $\sim$2.5 μm/s [23, 30, 36]. We note that ultrafast contractile velocities observed in protists such as *Spirostomum ambiguum*, which can reach 0.1 m/s [37, 43], involves a fishnet arrangement of Ca^{2+}-binding proteins homologous to Tcb2 with a secondary scaffolding protein [49]. In future work it may be possible to refine the *in vitro* system to account for these biological details to reach similar speeds. Third, this system has a minimal chemical composition, containing just three key components: Ca^{2+} (which serves as a bioorthogonal fuel compared to ATP), competing chelator molecules, and Tcb2 protein. In contrast, in most reconstituted actomyosin networks there are several additional accessory proteins and crowding agents that are typically used to regulate actin polymerization and confine filaments to a surface [83, 84].

The physics of this soft material presents several opportunities for model development, unification, and control. The system's mechanics are tightly coupled to its chemistry: diffusive network growth creates strong density inhomogeneities, and Ca^{2+} binding to Tcb2 alters the elastic rest length, necessitating extensions to standard viscoelasticity theory. The reversal of contractile forces due to these density inhomogeneities is a general physical phenomenon that may explain contractility in other systems like cytoskeletal networks [85]. Additionally, the coupling of stress generation to chemistry in our biomimetic system is reminiscent of earlier works on periodic swelling in synthetic polymer gels due to pattern-forming chemical reaction networks [2, 3], although these swelling motions are much slower. That pulsing the light activation allows for greater force generation through a recharging mechanism may be relevant to understanding the function of, for example, pulsatile dynamics in excitable RhoA-actin systems [86]. Finally, our efforts to control this soft material using reinforcement learning builds on a broader current research thrust of using control theory techniques to design policies that enable precise, on-demand force production in soft active matter systems [50, 51, 53, 54, 57].

This early demonstration of feasibility for controlling Tcb2 network dynamics points to the promise of using this system for applications in synthetic biology. Variants of caged DMNP-EDTA were previously used to increase cytoplasmic Ca^{2+} level *in vivo* to induce changes in keratocytes morphology and locomotion [87], suggesting that it may be possible to extend our approaches to control ultrafast contraction in living organisms. Of particular interest will be designing interactions between Tcb2 networks and lipid membranes, for example to create non-canonical cytoskeletal mimics of cytokinesis or endocytosis [79]. Additionally, intracellular transport of organelles may be feasible using Tcb2 networks. We also expect it will be possible to gain new biological insights into how ultrafast contraction occurs *in vivo* by reconstituting associated networks *in vitro*. This work suggests that the power of ultrafast contractility, occurring naturally in various heterotrich protists, may be harnessed as an externally-controllable material for subcellular control. This material may enable new nanoscale, Ca^{2+}-based, and light-actuatable synthetic force-generating cy-

toskeletal assemblies that may have applications in intracellular actuation and sensing, therapeutic drug delivery, and the development of artificial cytoskeletons. For synthetic cells, these supramolecular springs could introduce novel mechanical capabilities, including faster contraction than any microtubule- or actin-based system, localized force generation independent of polymer tracks, controllability that operates orthogonally to cell-specific biochemistry, and a unique energy source for intracellular movement that does not rely on ATP or GTP.

IV. METHODS AND MATERIALS

A. Tcb2 construction, storage, and purification

We synthesize a codon-optimized full-length version of the Tcb2 protein and clone it into a pJ411 expression plasmid, which we then transform into the BL21 strain of *E. coli* (see SI I C for sequence details). We synthesize GFP- and mCherry-tagged variants of Tcb2 to facilitate experiments shown in Fig. 1a. To prevent aggregation during storage, we store the synthesized proteins in 4 M urea solution at $-80°$C. Prior to experiments, we remove urea by overnight dialysis against a buffer containing 25 mM Tris (pH 7.5) and 1 mM EGTA, using a 3.5–5 kDa MWCO membrane (Spectra-Por Float-A-Lyzer G2, black). After dialysis, we concentrate the protein to approximately 30 mg/mL using a centrifugal filter (Amicon Ultra, UFC500324). We determine the final protein concentration by measuring absorbance at 280 nm with a UV spectrometer.

B. Light control technique

To ensure complete chelation of Ca^{2+}, we prepare a premixed solution of DMNP-EDTA and Ca^{2+} in a 2:1 molar ratio, with final concentrations of 0.54 mM Tcb2, 6.8 mM DMNP-EDTA and 3.4 mM Ca^{2+}. We prepare the sample in a "sandwich structure" with a glass slide, a coverslip and a spacer (9 × 9 mM, 25 μL; BioRad, SLF0201) to maintain precise height. We perform imaging using a Nikon Ti2 Eclipse inverted microscope with a 20× and 40× objective. To initiate the release of Ca^{2+} from the DMNP-EDTA-Ca^{2+} complex, we project a 365 nm light pattern through a Mightex Polygon 1000-G DMD (SI I D).

C. Liposome formation

We prepare liposomes using the cDICE method [88] with EggPC (840051P, Avanti Polar Lipids) and an osmotic pressure difference of 10 mOsm/kg between the inner and outer solutions. The inner solution contains 290 mOsm/kg glucose, while the outer solution contains 300 mOsm/kg sucrose in ultrapure MQ water. We centrifuge the resulting aqueous phase containing liposomes at 1000 rpm for 5 minutes to concentrate the liposomes at the bottom of the sample due to the density difference between the inner and outer solutions. We then transfer the 2 μL aliquot from the concentrated liposome layer to a 30 mg/mL Tcb2 solution in a 10% v/v ratio, resulting in a total solution volume of 20 μL. We place the mixture on a glass slide that has been pretreated with a 10 mg/mL poly-L-lysine hydrobromide solution [25, 89]. The lipids particles shown in Fig. 5b are the byproducts of liposomes preparation [90]. We then prepare the sample in the same "sandwich structure" as described in Methods IV B.

D. PIV analysis and particle preparation

We segment DIC videos using the AI model Segment Anything [91, 92] to track the growth of the Tcb2 network. We employ the prompt-based initialization model to enhance segmentation speed and accuracy for the Tcb2 network. For PIV analysis, we adapt the PIV MATLAB code to track Tcb2 filaments [93], with images preprocessed using a Gaussian filter (standard deviation: 12 pixels) and tracked using a nearest-neighbor algorithm within a search window grid of 48 pixels. We perform tracking and trajectory analysis of liposomes, lipid particles, and fluorescent particles using the AI tool CoTracker, with a manually set initial prompt-point and a grid size of 50 pixels [94]. We use 10-22 μm Fluorescent Red Polyethylene Microspheres (cospheric UVPMS-BR-0.995) for SI video Section VI.

E. Continuum model

Our chemomechanical model uses reaction-diffusion dynamics, for the evolution of the chemical concentration fields coupled to an overdamped elastic solid for the evolution of the displacement fields, whose density and rest strain depend on local chemical concentrations (SI I E). The external light field is a treated as a non-autonomous source function in the model whose magnitude spatiotemporally sets the rate of Ca^{2+} release by DMNP-EDTA. We distinguish between diffusing and bound Tcb2, as well as between Ca^{2+}-bound and unbound Tcb2. As a first approximation, we assume a simple model for nucleation and growth of the Tcb2 network, in which available Tcb2 binding sites depend non-monotonically on the local concentration of bound Tcb2 to capture the competing effects of bound Tcb2 concentration locally creating new binding sites while also contributing to steric interference. Ca^{2+}-induced growth of the bound network is modeled by taking the unbinding rate of Ca^{2+}-bound Tcb2 from the network to be significantly less than that of Tcb2 not bound to Ca^{2+}. We incorporate the degradation of DMNP-EDTA upon photolysis as a fractional

contribution to the viable DMNP-EDTA concentration following Ca^{2+} release. For simplicity we neglect possible advection of diffusing particles by motion of the network. To accelerate calculations for azimuthally symmetric light patterns we solve the equations of motion in cylindrical coordinates and neglect the angular dependence. We constrain parameterization of the model by the known reaction rates and otherwise determine parameters through exploration to produce dynamics which match the experimental observables. We give parameter values in SI I E.

F. Simulation methods

To integrate the dynamical equations we developed custom Julia code which implements Heun's method, a finite difference predictor-corrector scheme. We impose no-flux Neumann boundary conditions for the chemical species, preventing them from diffusing away from the simulation volume. We impose Dirichlet conditions $\mathbf{u} = \mathbf{0}$ for the displacement field at the boundary. We choose sufficiently fine spatial and temporal discretization to ensure numerical stability and convergence.

G. Reinforcement learning

We define the RL learning task in terms of an imposed dynamical law on the displacement $u(r_0, t)$ at at fixed radial coordinate r_0 of the material. We use RL to learn a mapping (called a policy) from $u(r_0, t)$ to the radius of the azimuthally-symmetric sigmoidal light profile and its amplitude. This mapping should mimic the dynamics of an overdamped spring connecting the displacement at position r_0 to the target displacement u_{goal}. We vary u_{goal} to test the ability to learn different dynamical tasks, as in our previous work on active nematics [57]. We train the system using the deep deterministic policy gradient algorithm (DDPG), which is a variant of the actor-critic method [76, 95, 96]. For this we combine our custom numerical integrator of the Tcb2 dynamics with the DDPG implementation provided by the Julia package ReinforcementLearning.jl [97]. Additional details of the RL problem formulation and training algorithm are given in SI I F.

ACKNOWLEDGMENTS

We wish to thank Douglas Chalker for providing the Tcb2-GFP tagged *Tetrahymena* strain, Heidi Sleister and students for creating the GFP/mCherry versions of Tcb2 and Mary Elting, Fred Chang, Jane Maienschein, and Suri Vaikuntanathan for helpful discussions. We also acknowledge the use of ChatGPT to refine the language in the supplementary information. A.R.D. acknowledges support from National Science Foundation (NSF) award 2313725 and the University of Chicago Materials Research Science and Engineering Center funded by NSF award 2011854. S.C. acknowledges support from NSF award 2313723 and the David and Lucille Packard Fellowship for Science and Engineering. J.H. acknowledges support from NSF award 2313727. S.B. acknowledges support from NSF award MCB-2313724 and National Institutes of Health (NIH) award R35GM142588. The authors acknowledge the University of Chicago's Research Computing Center for computing resources.

[1] G. Gompper, H. A. Stone, C. Kurzthaler, D. Saintillan, F. Peruani, D. A. Fedosov, T. Auth, C. Cottin-Bizonne, C. Ybert, E. Clement, T. Darnige, A. Lindner, R. E. Goldstein, B. Liebchen, J. Binysh, A. Souslov, L. Isa, R. di Leonardo, G. Frangipane, H. Gu, B. J. Nelson, F. Brauns, M. C. Marchetti, F. Cichos, V.-L. Heuthe, C. Bechinger, A. Korman, O. Feinerman, A. Cavagna, I. Giardina, H. Jeckel, and K. Drescher, The 2024 motile active matter roadmap, arXiv [cond-mat.soft] (2024).

[2] V. V. Yashin and A. C. Balazs, Pattern formation and shape changes in self-oscillating polymer gels, Science **314**, 798 (2006).

[3] R. Yoshida, Self-oscillating gels driven by the belousov–zhabotinsky reaction as novel smart materials, Advanced Materials **22**, 3463 (2010).

[4] A. Grinthal and J. Aizenberg, Adaptive all the way down: building responsive materials from hierarchies of chemomechanical feedback, Chem. Soc. Rev. **42**, 7072 (2013).

[5] B. Blanc, Z. Zhang, E. Liu, N. Zhou, I. Dellatolas, A. Aghvami, H. Yi, and S. Fraden, Active pulsatile gels: From a chemical microreactor to a polymeric actuator, Langmuir **40**, 6862 (2024).

[6] B. Blanc, J. N. Agyapong, I. Hunter, J.-C. Galas, A. Fernandez-Nieves, and S. Fraden, Collective chemomechanical oscillations in active hydrogels, Proceedings of the National Academy of Sciences **121**, e2313258121 (2024).

[7] L. Xue, X. Xiong, B. P. Krishnan, F. Puza, S. Wang, Y. Zheng, and J. Cui, Light-regulated growth from dynamic swollen substrates for making rough surfaces, Nature communications **11**, 963 (2020).

[8] M. Chen, M. Zhong, and J. A. Johnson, Light-controlled radical polymerization: mechanisms, methods, and applications, Chemical reviews **116**, 10167 (2016).

[9] G. M. Whitesides and B. Grzybowski, Self-assembly at all scales, Science **295**, 2418 (2002).

[10] R. Freeman, M. Han, Z. Álvarez, J. A. Lewis, J. R. Wester, N. Stephanopoulos, M. T. McClendon, C. Lynsky, J. M. Godbe, H. Sangji, *et al.*, Reversible self-assembly of superstructured networks, Science **362**, 808 (2018).

[11] Y.-K. Kim, X. Wang, P. Mondkar, E. Bukusoglu, and N. L. Abbott, Self-reporting and self-regulating liquid crystals, Nature **557**, 539 (2018).

[12] S. Li, B. Deng, A. Grinthal, A. Schneider-Yamamura, J. Kang, R. S. Martens, C. T. Zhang, J. Li, S. Yu, K. Bertoldi, and J. Aizenberg, Liquid-induced topological transformations of cellular microstructures, Nature **592**, 386 (2021).

[13] S. Liu, S. Shankar, M. C. Marchetti, and Y. Wu, Viscoelastic control of spatiotemporal order in bacterial active matter, Nature **590**, 80 (2021).

[14] A. Sokolov, M. M. Apodaca, B. A. Grzybowski, and I. S. Aranson, Swimming bacteria power microscopic gears, Proceedings of the National Academy of Sciences **107**, 969 (2010).

[15] H. Gu, Q. Boehler, H. Cui, E. Secchi, G. Savorana, C. De Marco, S. Gervasoni, Q. Peyron, T.-Y. Huang, S. Pane, *et al.*, Magnetic cilia carpets with programmable metachronal waves, Nature communications **11**, 2637 (2020).

[16] W. Wang, Q. Liu, I. Tanasijevic, M. F. Reynolds, A. J. Cortese, M. Z. Miskin, M. C. Cao, D. A. Muller, A. C. Molnar, E. Lauga, *et al.*, Cilia metasurfaces for electronically programmable microfluidic manipulation, Nature **605**, 681 (2022).

[17] T. Sanchez, D. T. N. Chen, S. J. DeCamp, M. Heymann, and Z. Dogic, Spontaneous motion in hierarchically assembled active matter, Nature **491**, 431 (2012).

[18] V. Schaller, C. Weber, C. Semmrich, E. Frey, and A. R. Bausch, Polar patterns of driven filaments, Nature **467**, 73 (2010).

[19] C. G. Muresan, Z. G. Sun, V. Yadav, A. P. Tabatabai, L. Lanier, J. H. Kim, T. Kim, and M. P. Murrell, F-actin architecture determines constraints on myosin thick filament motion, Nat. Commun. **13**, 7008 (2022).

[20] V. Yadav, D. S. Banerjee, A. P. Tabatabai, D. R. Kovar, T. Kim, S. Banerjee, and M. P. Murrell, Filament nucleation tunes mechanical memory in active polymer networks, Adv. Funct. Mater. **29** (2019).

[21] I. Linsmeier, S. Banerjee, P. W. Oakes, W. Jung, T. Kim, and M. P. Murrell, Disordered actomyosin networks are sufficient to produce cooperative and telescopic contractility, Nat. Commun. **7**, 12615 (2016).

[22] S. A. Redford, J. Colen, J. L. Shivers, S. Zemsky, M. Molaei, C. Floyd, P. V. Ruijgrok, V. Vitelli, Z. Bryant, A. R. Dinner, and M. L. Gardel, Motor crosslinking augments elasticity in active nematics, Soft Matter **20**, 2480 (2024).

[23] L. M. Lemma, M. Varghese, T. D. Ross, M. Thomson, A. Baskaran, and Z. Dogic, Spatio-temporal patterning of extensile active stresses in microtubule-based active fluids, PNAS nexus **2**, pgad130 (2023).

[24] M. Murrell, P. W. Oakes, M. Lenz, and M. L. Gardel, Forcing cells into shape: the mechanics of actomyosin contractility, Nat. Rev. Mol. Cell Biol. **16**, 486 (2015).

[25] R. Sakamoto, M. Tanabe, T. Hiraiwa, K. Suzuki, S. Ishiwata, Y. T. Maeda, and M. Miyazaki, Tug-of-war between actomyosin-driven antagonistic forces determines the positioning symmetry in cell-sized confinement, Nat. Commun. **11**, 3063 (2020).

[26] R. Sakamoto, Z. Izri, Y. Shimamoto, M. Miyazaki, and Y. T. Maeda, Geometric trade-off between contractile force and viscous drag determines the actomyosin-based motility of a cell-sized droplet, Proc. Natl. Acad. Sci. U. S. A. **119**, e2121147119 (2022).

[27] R. Adkins, I. Kolvin, Z. You, S. Witthaus, M. C. Marchetti, and Z. Dogic, Dynamics of active liquid interfaces, Science **377**, 768 (2022).

[28] I. Linsmeier, S. Banerjee, P. W. Oakes, W. Jung, T. Kim, and M. P. Murrell, Disordered actomyosin networks are sufficient to produce cooperative and telescopic contractility, Nature communications **7**, 12615 (2016).

[29] P. V. Ruijgrok, R. P. Ghosh, S. Zemsky, M. Nakamura, R. Gong, L. Ning, R. Chen, V. T. Vachharajani, A. E. Chu, N. Anand, R. R. Eguchi, P.-S. Huang, M. Z. Lin, G. M. Alushin, J. T. Liphardt, and Z. Bryant, Optical control of fast and processive engineered myosins in vitro and in living cells, Nat. Chem. Biol. **17**, 540 (2021).

[30] T. D. Ross, H. J. Lee, Z. Qu, R. A. Banks, R. Phillips, and M. Thomson, Controlling organization and forces in active matter through optically defined boundaries, Nature **572**, 224 (2019).

[31] M. Malik-Garbi, N. Ierushalmi, S. Jansen, E. Abu-Shah, B. L. Goode, A. Mogilner, and K. Keren, Scaling behaviour in steady-state contracting actomyosin networks, Nat. Phys. **15**, 509 (2019).

[32] P. W. Oakes, E. Wagner, C. A. Brand, D. Probst, M. Linke, U. S. Schwarz, M. Glotzer, and M. L. Gardel, Optogenetic control of RhoA reveals zyxin-mediated elasticity of stress fibres, Nat. Commun. **8**, 15817 (2017).

[33] M. Schuppler, F. C. Keber, M. Kröger, and A. R. Bausch, Boundaries steer the contraction of active gels, Nat. Commun. **7**, 13120 (2016).

[34] K. E. Cavanaugh, P. W. Oakes, and M. L. Gardel, Optogenetic control of RhoA to probe subcellular mechanochemical circuitry, Curr. Protoc. Cell Biol. **86**, e102 (2020).

[35] S. Chandrasekar, J. R. Beach, and P. W. Oakes, Shining a light on rhoa: Optical control of cell contractility, The International Journal of Biochemistry & Cell Biology **161**, 106442 (2023).

[36] Z. Qu, D. Schildknecht, S. Shadkhoo, E. Amaya, J. Jiang, H. J. Lee, D. Larios, F. Yang, R. Phillips, and M. Thomson, Persistent fluid flows defined by active matter boundaries, Communications Physics **4**, 1 (2021).

[37] A. J. T. M. Mathijssen, J. Culver, M. S. Bhamla, and M. Prakash, Collective intercellular communication through ultra-fast hydrodynamic trigger waves, Nature **571**, 560 (2019).

[38] F. Ruiz, N. Garreau de Loubresse, C. Klotz, J. Beisson, and F. Koll, Centrin deficiency in paramecium affects the geometry of basal-body duplication, Curr. Biol. **15**, 2097 (2005).

[39] L. Mahadevan and P. Matsudaira, Motility powered by supramolecular springs and ratchets, Science **288**, 95 (2000).

[40] R. B. Hawkes and D. V. Holberton, Myonemal contraction of spirostomum. i. kinetics of contraction and relaxation, J. Cell. Physiol. **84**, 225 (1974).

[41] G. Misra, R. B. Dickinson, and A. J. C. Ladd, Mechanics of vorticella contraction, Biophys. J. **98**, 2923 (2010).

[42] A. M. Kilpatrick, J. E. Honts, H. M. Sleister, and C. A. Fowler, Solution NMR structures of the C-domain of tetrahymena cytoskeletal protein Tcb2 reveal distinct calcium-induced structural rearrangements, Proteins **84**, 1748 (2016).

[43] C. Floyd, A. T. Molines, X. Lei, J. E. Honts, F. Chang, M. W. Elting, S. Vaikuntanathan, A. R. Dinner, and M. S. Bhamla, A unified model for the dynamics of atp-

independent ultrafast contraction, Proceedings of the National Academy of Sciences **120**, e2217737120 (2023).

[44] A. Upadhyaya, M. Baraban, J. Wong, P. Matsudaira, A. Van Oudenaarden, and L. Mahadevan, Power-limited contraction dynamics of vorticella convallaria: an ultrafast biological spring, Biophysical Journal **94**, 265 (2008).

[45] E. G. Chung and S. Ryu, Stalk-length-dependence of the contractility of vorticella convallaria, Physical Biology **14**, 066002 (2017).

[46] S. Ryu, M. J. Lang, and P. Matsudaira, Maximal force characteristics of the ca2+-powered actuator of vorticella convallaria, Biophysical journal **103**, 860 (2012).

[47] R. Chang and M. Prakash, Topological damping in an ultrafast giant cell, Proceedings of the National Academy of Sciences **120**, e2303940120 (2023).

[48] R. Chang and M. Prakash, Biophysical limits of ultrafast cellular motility, bioRxiv , 2024 (2024).

[49] J. Lannan, C. Floyd, L. Xu, C. Yan, W. F. Marshall, S. Vaikuntanathan, A. R. Dinner, J. E. Honts, S. Bhamla, and M. W. Elting, Fishnet mesh of centrin-sfi1 drives ultrafast calcium-activated contraction of the giant cell spirostomum ambiguum, bioRxiv , 2024 (2024).

[50] M. M. Norton, P. Grover, M. F. Hagan, and S. Fraden, Optimal control of active nematics, Physical review letters **125**, 178005 (2020).

[51] S. Ghosh, C. Joshi, A. Baskaran, and M. F. Hagan, Spatiotemporal control of structure and dynamics in a polar active fluid, arXiv e-prints , arXiv (2024).

[52] S. Ghosh, A. Baskaran, and M. F. Hagan, Achieving designed texture and flows in bulk active nematics using optimal control theory, arXiv preprint arXiv:2408.14596 (2024).

[53] C. G. Wagner, M. M. Norton, J. S. Park, and P. Grover, Exact coherent structures and phase space geometry of preturbulent 2d active nematic channel flow, Physical Review Letters **128**, 028003 (2022).

[54] K. Nishiyama, J. Berezney, M. M. Norton, A. Aggarwal, S. Ghosh, M. F. Hagan, Z. Dogic, and S. Fraden, Closed-loop control of active nematic flows, arXiv preprint arXiv:2408.14414 (2024).

[55] S. Shankar, L. V. Scharrer, M. J. Bowick, and M. C. Marchetti, Design rules for controlling active topological defects, Proceedings of the National Academy of Sciences **121**, e2400933121 (2024).

[56] C. Floyd, A. R. Dinner, and S. Vaikuntanathan, Learning to control non-equilibrium dynamics using local imperfect gradients, arXiv preprint arXiv:2404.03798 (2024).

[57] C. Floyd, A. R. Dinner, and S. Vaikuntanathan, Tailoring interactions between active nematic defects with reinforcement learning, arXiv preprint arXiv:2411.09588 (2024).

[58] T. Takemasa, K. Ohnishi, T. Kobayashi, T. Takagi, K. Konishi, and Y. Watanabe, Cloning and sequencing of the gene for tetrahymena calcium-binding 25-kda protein (TCBP-25)*, Journal of Biological Chemistry **264**, 19293 (1989).

[59] A. M. Kilpatrick, T. E. Gurrola, R. C. Sterner, H. M. Sleister, J. E. Honts, and C. A. Fowler, Backbone and side-chain chemical shift assignments for the c-terminal domain of tcb2, a cytoskeletal calcium-binding protein from tetrahymena thermophila, Biomol. NMR Assign. **10**, 281 (2016).

[60] K. Hanyu, T. Takemasa, O. Numata, M. Takahashi, and Y. Watanabe, Immunofluorescence localization of a 25-kda tetrahymena ef-hand ca2+-binding protein, tcbp-25, in the cell cortex and possible involvement in conjugation, Experimental cell research **219**, 487 (1995).

[61] T. Nakagawa, K. Fujiu, E. S. Cole, and O. Numata, Involvement of a 25 kDa Tetrahymena Ca2+-binding protein in pronuclear exchange, Cell structure and function **33**, 151 (2008).

[62] R. Chang and M. Prakash, Biophysical limits of ultrafast cellular motility, bioRxiv (2024).

[63] K. Ohnishi and Y. Watanabe, Purification and some properties of a new Ca2+-binding protein (TCBP-10) present in tetrahymena cilium, J. Biol. Chem. **258**, 13978 (1983).

[64] J. Abramson, J. Adler, J. Dunger, R. Evans, T. Green, A. Pritzel, O. Ronneberger, L. Willmore, A. J. Ballard, J. Bambrick, S. W. Bodenstein, D. A. Evans, C.-C. Hung, M. O'Neill, D. Reiman, K. Tunyasuvunakool, Z. Wu, A. Žemgulytė, E. Arvaniti, C. Beattie, O. Bertolli, A. Bridgland, A. Cherepanov, M. Congreve, A. I. Cowen-Rivers, A. Cowie, M. Figurnov, F. B. Fuchs, H. Gladman, R. Jain, Y. A. Khan, C. M. R. Low, K. Perlin, A. Potapenko, P. Savy, S. Singh, A. Stecula, A. Thillaisundaram, C. Tong, S. Yakneen, E. D. Zhong, M. Zielinski, A. Žídek, V. Bapst, P. Kohli, M. Jaderberg, D. Hassabis, and J. M. Jumper, Accurate structure prediction of biomolecular interactions with AlphaFold 3, Nature **630**, 493 (2024).

[65] J. E. Honts and N. E. Williams, Novel cytoskeletal proteins in the cortex of tetrahymena1, J. Eukaryot. Microbiol. **50**, 9 (2003).

[66] C.-F. Yang and W.-C. Tsai, Calmodulin: The switch button of calcium signaling: The switch button of calcium signaling, Tzu Chi Med. J. **34**, 15 (2022).

[67] DMNP-EDTA, tetrapotassium salt (caged calcium), `https://biotium.com/product/dmnp-edta-tetrapotassium-salt-caged-calcium/` (2016), accessed: 2024-6-3.

[68] D. M. Bers, C. W. Patton, and R. Nuccitelli, A practical guide to the preparation of ca, A practical guide to the study of calcium in living cells **40**, 3 (1994).

[69] O. L. Barreto-Chang and R. E. Dolmetsch, Calcium imaging of cortical neurons using fura-2 AM, J. Vis. Exp. (2009).

[70] R. Tsien and T. Pozzan, [14] measurement of cytosolic free ca2+ with quin2, in *Methods in Enzymology*, Vol. 172 (Academic Press, 1989) pp. 230–262.

[71] J. Bechhoefer, *Control theory for physicists* (Cambridge University Press, 2021).

[72] Polygon: Cellular-Resolution optogenetics & photostimulation, `https://www.mightexbio.com/polygon/` (2017), accessed: 2024-6-5.

[73] N. Phan-Thien and N. Mai-Duy, *Understanding viscoelasticity: an introduction to rheology* (Springer, 2013).

[74] M. F. Ashby and D. Cebon, Materials selection in mechanical design, Le Journal de Physique IV **3**, C7 (1993).

[75] X. Li, Q. Ni, X. He, J. Kong, S.-M. Lim, G. A. Papoian, J. P. Trzeciakowski, A. Trache, and Y. Jiang, Tensile force-induced cytoskeletal remodeling: Mechanics before chemistry, PLoS computational biology **16**, e1007693 (2020).

[76] R. S. Sutton and A. G. Barto, *Reinforcement Learning: An Introduction* (MIT press, 2018).

[77] C. Floyd, H. Levine, C. Jarzynski, and G. A. Papoian, Understanding cytoskeletal avalanches using mechanical

stability analysis, Proc. Natl. Acad. Sci. U. S. A. **118**, e2110239118 (2021).

[78] M. Vicente-Manzanares, X. Ma, R. S. Adelstein, and A. R. Horwitz, enNon-muscle myosin II takes centre stage in cell adhesion and migration, Nat. Rev. Mol. Cell Biol. **10**, 778 (2009).

[79] R. Sakamoto and M. P. Murrell, Mechanical power is maximized during contractile ring-like formation in a biomimetic dividing cell model, Nature communications **15**, 9731 (2024).

[80] M. Soares e Silva, M. Depken, B. Stuhrmann, M. Korsten, F. C. MacKintosh, and G. H. Koenderink, Active multistage coarsening of actin networks driven by myosin motors, Proc. Natl. Acad. Sci. U. S. A. **108**, 9408 (2011).

[81] J. A. Wagoner and K. A. Dill, Evolution of mechanical cooperativity among myosin II motors, Proc. Natl. Acad. Sci. U. S. A. **118**, e2101871118 (2021).

[82] A. Krishna, M. Savinov, N. Ierushalmi, A. Mogilner, and K. Keren, Size-dependent transition from steady contraction to waves in actomyosin networks with turnover (2022).

[83] P. K. Mattila and P. Lappalainen, Filopodia: molecular architecture and cellular functions, Nat. Rev. Mol. Cell Biol. **9**, 446 (2008).

[84] M. P. Murrell and M. L. Gardel, F-actin buckling coordinates contractility and severing in a biomimetic actomyosin cortex, Proc. Natl. Acad. Sci. U. S. A. **109**, 20820 (2012).

[85] M. Lenz, Reversal of contractility as a signature of self-organization in cytoskeletal bundles, Elife **9**, e51751 (2020).

[86] W. M. Bement, M. Leda, A. M. Moe, A. M. Kita, M. E. Larson, A. E. Golding, C. Pfeuti, K.-C. Su, A. L. Miller, A. B. Goryachev, *et al.*, Activator–inhibitor coupling between rho signalling and actin assembly makes the cell cortex an excitable medium, Nature cell biology **17**, 1471 (2015).

[87] A. Ishihara, K. Gee, S. Schwartz, K. Jacobson, and J. Lee, Photoactivation of caged compounds in single living cells: an application to the study of cell locomotion, Biotechniques **23**, 268 (1997).

[88] M. C. Blosser, B. G. Horst, and S. L. Keller, cDICE method produces giant lipid vesicles under physiological conditions of charged lipids and ionic solutions, Soft Matter **12**, 7364 (2016).

[89] M. Abkarian, E. Loiseau, and G. Massiera, Continuous droplet interface crossing encapsulation (cDICE) for high throughput monodisperse vesicle design, Soft Matter **7**, 4610 (2011).

[90] A. Moga, N. Yandrapalli, R. Dimova, and T. Robinson, Optimization of the inverted emulsion method for high-yield production of biomimetic giant unilamellar vesicles, Chembiochem **20**, 2674 (2019).

[91] A. Kirillov, E. Mintun, N. Ravi, H. Mao, C. Rolland, L. Gustafson, T. Xiao, S. Whitehead, A. C. Berg, W.-Y. Lo, P. Dollár, and R. Girshick, Segment anything, arXiv:2304.02643 (2023).

[92] K. Nar, segment-anything-video: MetaSeg: Packaged version of the segment anything repository.

[93] W. Thielicke and R. Sonntag, Particle image velocimetry for MATLAB: Accuracy and enhanced algorithms in PIVlab, J. Open Res. Softw. **9**, 12 (2021).

[94] N. Karaev, I. Rocco, B. Graham, N. Neverova, A. Vedaldi, and C. Rupprecht, Cotracker: It is better to track together, in *Proc. ECCV* (2024).

[95] D. Silver, G. Lever, N. Heess, T. Degris, D. Wierstra, and M. Riedmiller, Deterministic policy gradient algorithms, in *International conference on machine learning* (Pmlr, 2014) pp. 387–395.

[96] T. P. Lillicrap, J. J. Hunt, A. Pritzel, N. Heess, T. Erez, Y. Tassa, D. Silver, and D. Wierstra, Continuous control with deep reinforcement learning, arXiv preprint arXiv:1509.02971 (2015).

[97] J. Tian and other contributors, Reinforcementlearning.jl: A reinforcement learning package for the julia programming language (2020).